



Publication Year	2015
Acceptance in OA @INAF	2020-07-22T10:07:18Z
Title	Self-Tuning Mechanism for the Design of Adaptive Secondary Mirror Position Control
Authors	Battistelli, Giorgio; Mari, Daniele; RICCARDI, Armando; Tesi, Pietro
DOI	10.1109/TCST.2015.2398822
Handle	http://hdl.handle.net/20.500.12386/26569
Journal	IEEE TRANSACTIONS ON CONTROL SYSTEMS TECHNOLOGY
Number	23

Self-Tuning Mechanism for the Design of Adaptive Secondary Mirror Position Control

Giorgio Battistelli, Daniele Mari, Armando Riccardi, and Pietro Tesi

Abstract—Deformable mirrors (DMs) are electromechanical devices used in ground-based telescopes to compensate for the distortions caused by the atmospheric turbulence, the main factor limiting the resolution of astronomical imaging. Adaptive secondary mirrors (ASMs) represent a new type of DMs; two of them have been recently installed on the 8-m-class large binocular telescope (LBT). ASMs are able to jointly correct rigid and nonrigid wave-front distortions thanks to the use of force actuators distributed on the overall mirror surface. As an offset, each actuator needs to be piloted by a dedicated controller, whose parameters must be accurately tuned to obtain the desired mirror shape. At the present time, the calibration of the controller parameters is executed manually. This paper presents a novel automatic controller tuning procedure that does not rely on the modeling of the mirror dynamics. The experimental validation on a prototype reproducing the three innermost rings of the LBT ASM is reported.

Index Terms—Adaptive optics (AO), adaptive secondary mirrors (ASMs), decentralized feedback control, reference model design, self-tuning control, unfalsified control, virtual experiment.

I. INTRODUCTION

ADAPTIVE OPTICS (AO) is a technology used nowadays in ground-based telescopes to compensate for the distortions caused by the atmospheric turbulence (*seeing*), the factor that mainly affects the resolution of astronomical imaging. AO systems consist of three main elements: a sensor unit, called the wave front sensor (WFS), a deformable mirror (DM), and a real-time control unit, called the AO controller. As schematically represented in Fig. 1, the WFS measures the distortions caused by the atmospheric turbulence; using these measurements, the AO controller calculates the mirror shape that corrects the distortions and the surface of the DM is reshaped accordingly. Technology wise, several kinds of WFSs and DMs are currently used in AO. As for WFSs, common choices include Shack–Hartmann,

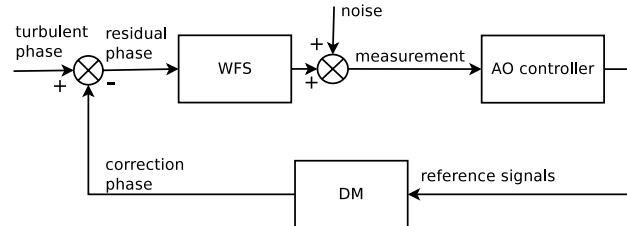


Fig. 1. Typical AO control system.

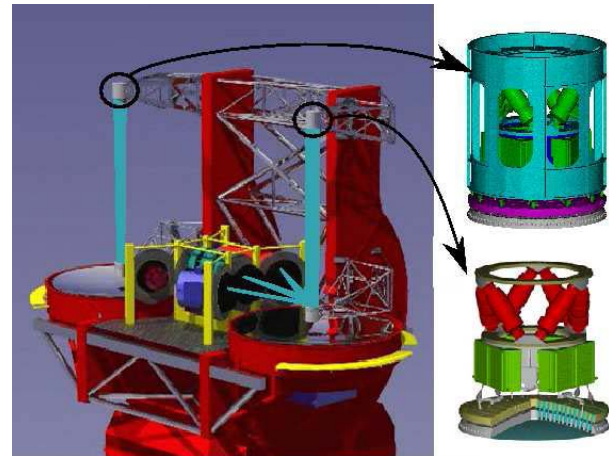


Fig. 2. ASMs' placement in LBT, Arizona, USA: each ASM serves three focal stations.

pyramid, and curvature sensors [1], [2]. As for DMs, a main distinction can be made among segmented continuous facesheet and bimorph mirrors [3]–[6].

This paper focuses on the design of the *internal control* for a class of DMs known as adaptive secondary mirrors (ASMs). ASMs represent a rather new and extremely promising generation of continuous facesheet mirrors, consisting of a thin-curved facesheet controlled by means of voice-coil actuators. ASMs offer several advantages compared with conventional DMs: a drastic reduction in the number of optical surfaces along the optical train, resulting in an AO system of a higher transmission and lower emissivity [7]; the possibility to serve multiple focal stations, as shown in Fig. 2; a stroke (of $\sim 100 \mu\text{m}$ versus $\sim 10 \mu\text{m}$ using piezoelectric actuators) large enough to compensate for rigid deformations [8]; less breaks/faults liability since the force applied to the mirror shell does not involve physical contacts [9]; the possibility, thanks to a high actuator density, to deal also with short-light wavelength [10]; and finally, the possibility to support

Manuscript received November 2, 2014; accepted December 31, 2014. Manuscript received in final form January 25, 2015. Recommended by Associate Editor A. Serrani.

G. Battistelli is with the Dipartimento di Ingegneria dell'Informazione, University of Florence, Florence 50121, Italy (e-mail: giorgio.battistelli@unifi.it).

D. Mari is with Positech Consulting S.r.l., Milan 20122, Italy (e-mail: danielle.mari@positech.it).

A. Riccardi is with Osservatorio Astrofisico di Arcetri, Florence 50125, Italy (e-mail: riccardi@arcetri.astro.it).

P. Tesi is with the ITM Group, Faculty of Mathematics and Natural Sciences, University of Groningen, Groningen 9712 CP, The Netherlands (e-mail: p.tesi@rug.nl).

Color versions of one or more of the figures in this paper are available online at <http://ieeexplore.ieee.org>.

Digital Object Identifier 10.1109/TCST.2015.2398822

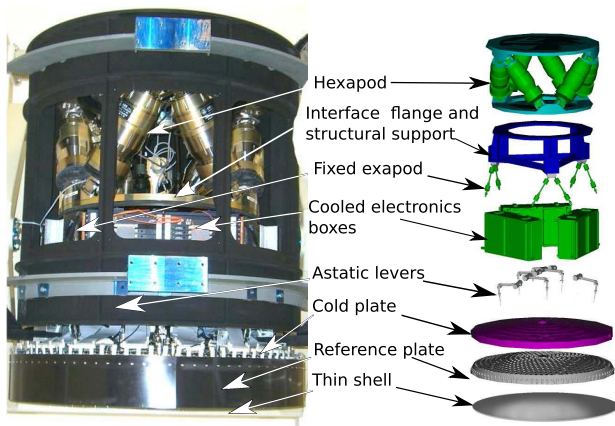


Fig. 3. Layout of one ASM of the LBT.

ground-layer and multiconjugate AO [11]–[13].

The first ASM was built for the 6-m-class multiple mirror telescope, Arizona, USA, in the mid-1990s [14], [15]. Thereafter, two ASMs were installed on the large binocular telescope (LBT), Arizona, USA, by a joint collaboration among several partners, including the Arcetri Astrophysical Observatory, Italy, Microgate s.r.l., Italy, ADS International s.r.l., Italy, the Department of Aerospace Engineering, Politecnico di Milano, Italy, and the Steward Observatory, University of Arizona, USA. Fig. 3 shows the layout of one LBT ASM [16]. It consists of a ~ 2 -mm-thick DM (*shell*) with a ~ 1 -m diameter, a thick plate that provides the reference surface (*reference plate*), a third plate (*cold plate*) that supports and cools the actuators, the actuators, and the sensors. The shell has a 5-cm diameter central hole where a mechanical support is placed; this gives a constraint that blocks the motions of the shell on its plane and is weak in the orthogonal direction. There are 672 voice-coil force actuators, distributed over 14 concentric rings. They keep the shell in magnetic levitation so that, thanks to the weak constraint given by the support, the shell is able to achieve rigid deformations. For each actuator, there is a collocated capacitive sensor that measures the local distance between the shell and the reference plate.

A. ASM Control Design

Unlike classical DMs, where position (i.e., piezoelectric) actuators are controlled by the AO loop itself [4], ASMs require a dedicated control loop, known as *internal position control* loop. This constitutes the main subject of this paper. In this respect, while the analysis will primarily focus on the ASMs for the LBT, much of the considerations to follow apply to a generic ASMs as well.

The general scheme of an AO control system based on ASMs can be schematically represented as in Fig. 4 and involves an outer control loop (working at 1 kHz in the LBT case), which determines the commands to the ASM, and an inner control loop (the ASM internal position control, working at 72 kHz in the LBT case), which is responsible for shaping the mirror surface. As detailed in Section II, the inner control loop typically relies on a decentralized feedback plus

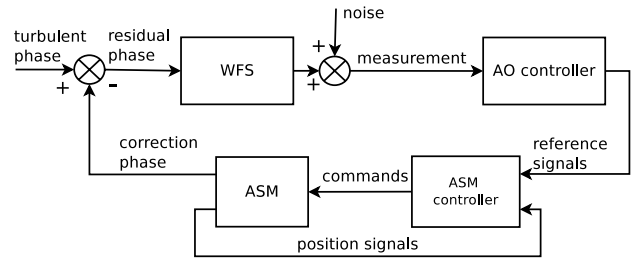


Fig. 4. ASM internal control loop in an AO system.

a centralized feedforward term. The decentralized component offers the definite advantage of scalability. Such a feature makes this solution well suited also for the next generation of telescopes, such as the GMT and the >20 -m-class extremely large telescopes [17]–[19] that will require a very large number of actuators. The feedforward contribution is instead adopted so as to guarantee a satisfactory steady-state error to step inputs. This is because the use of an integral action in the feedback path typically introduce unacceptable overshoots in the closed-loop response [20]. An alternative approach that considers the use of a feedforward contribution plus a centralized integral feedback action has been recently proposed in [21] and [22].

The control architecture based on decentralized feedback plus centralized feedforward has been shown to be highly performing and well suited for real-time implementation [20], [23], and is indeed currently adopted for the LBT. However, at the present moment, the design of a control architecture of this kind mainly relies on designers' experience. Specifically, while many efficient methods are available for computing the centralized feedforward action [23]–[25], few results are available for designing the decentralized feedback action. This is mainly due to the following factors: 1) the decentralized nature of the feedback action for which standard design tools are less available [26] and 2) the difficulty to obtain an accurate model of the shell dynamics. This is not the case for the centralized feedforward action, whose computation only requires information about the shell static behavior, the so-called shell stiffness matrix.

Prompted by these considerations, this paper considers a new approach to the design of the decentralized feedback for ASMs. The considered approach relies on the concept of *virtual experiment*, as originally proposed in [27] and refined in [28]–[32] in the context of switching adaptive control, and enjoys the following features:

- 1) It is *model free*, i.e., the control design does not require the identification of a model describing the shell dynamics.
- 2) It is *global* in the sense that it views the multiple-input multiple-output system dynamics and its interactions as a whole, which avoids the need for analyzing and designing the local control units separately.
- 3) It is *batch-wise* in the sense that the optimization procedure relies on a single data set, which is preliminarily collected on the mirror, thus reducing at minimum the interaction with the process.

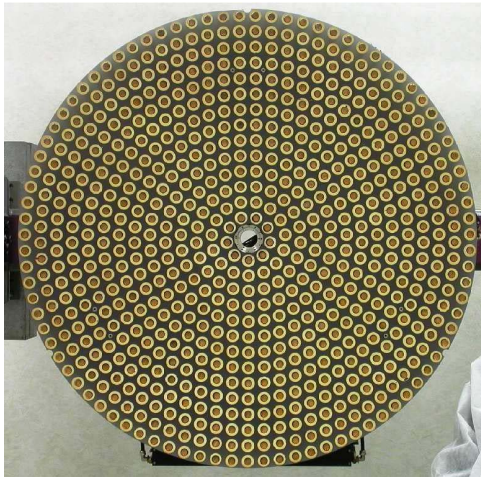


Fig. 5. Front view of the LBT reference plate. The 672 actuators are distributed in 14 concentric rings: the armatures of capacitive sensors collocated with actuators are visible.

These three features make the considered approach very appealing, especially with respect to the next generation of ground-based telescopes, which will make use of thousands of actuator/sensor pairs [33].

The remainder of this paper is as follows. In Section II, we describe the control architecture based on decentralized feedback plus centralized feedforward, and we formulate the control goal. The control design approach is described and discussed in Sections III and IV. Experimental results on the P45, a prototype reproducing the three innermost rings of the LBT ASM, are reported in Section V. Section VI ends this paper with concluding remarks.

II. INTERNAL POSITION CONTROL FOR ADAPTIVE SECONDARY MIRRORS

Section II-A describes the considered control architecture. Control goals and related design issues are discussed in Section II-B. While the analysis will primarily focus on the ASMs of the LBT, much of the considerations to follow apply to generic ASMs as well.

A. Control Architecture

The considered control architecture relies on the decentralized feedback plus centralized feedforward and is implemented on a digital platform. Both LBT ASMs are equipped with 168 digital signal processors, each working at 72 kHz and handling four pairs of actuators and collocated sensors, for a total of 672 actuator/sensor pairs. Omitting the sampling time for conciseness, the control action u can be represented in compact form as

$$\mathbf{u}(k) = \widehat{\mathbf{K}} \mathbf{r}(k) - \mathbf{K}_d \mathbf{H}(d) \mathbf{y}(k) + \mathbf{K}_p [\mathbf{r}(k) - \mathbf{y}(k)] \quad (1)$$

where \mathbf{u} , \mathbf{r} , and \mathbf{y} are all N -dimensional vectors, where N is the number of sensor/actuator pairs, arranged on a grid with circular geometry as in Fig. 5; the i th component of \mathbf{r} denotes the desired shell displacement $[m]$ (the distance between the

reference plate and the shell); the i th component of \mathbf{y} represents the actual shell displacement; the i th component of \mathbf{u} represents the force $[N]$ applied at the i th point of the grid; and $\mathbf{H}(d)$ is a diagonal matrix in the unit backward shift operator d . In particular, $\mathbf{H}(d) = H(d)\mathbf{I}_N$, where \mathbf{I}_N indicates the $N \times N$ identity matrix and $H(d)$ is a discrete approximation at low frequencies of the derivative action $\mathbf{K}_d d/dt$; it is obtained by applying the Tustin transformation to the continuous-time second-order overdamped filter

$$H(s) = \frac{s}{(1 + s/\omega_H)^2} \quad (2)$$

with cutoff frequency $\omega_H/(2\pi) = 15$ kHz in the case of both the LBT and the P45; $\widehat{\mathbf{K}}$, \mathbf{K}_p , and \mathbf{K}_d are $N \times N$ matrices detailed next.

The considered control architecture originates from the following considerations. As a very coarse approximation, the dynamics of the shell can be described by a continuous-time finite-dimensional system

$$\mathbf{M}\ddot{\mathbf{y}}(t) + \mathbf{D}\dot{\mathbf{y}}(t) + \mathbf{K}\mathbf{y}(t) = \mathbf{u}(t) \quad (3)$$

where \mathbf{M} , \mathbf{D} , and \mathbf{K} are the $N \times N$ matrices representing the mass, damping, and stiffness matrices of the shell, respectively. For example, an approximate model of this form can be obtained as a lumped element model or, alternatively, via the finite-element method (FEM) by considering the sensor/actuator locations as vertices of an FEM mesh.

Further, at low frequencies, the discrete-time control law (1) approximates the continuous-time control law

$$\mathbf{u}(t) = \widehat{\mathbf{K}} \mathbf{r}(t) - \mathbf{K}_d \dot{\mathbf{y}}(t) + \mathbf{K}_p [\mathbf{r}(t) - \mathbf{y}(t)].$$

Hence, denoting the Laplace operator by s , the control action approximately achieves the following transfer matrix $\mathbf{W}(s)$ from \mathbf{r} to \mathbf{y} :

$$\mathbf{W}(s) = [\mathbf{M}s^2 + (\mathbf{D} + \mathbf{K}_d)s + \mathbf{K}_p + \mathbf{K}]^{-1}(\mathbf{K}_p + \widehat{\mathbf{K}}). \quad (4)$$

One can therefore observe the following.

- 1) The role of $\widehat{\mathbf{K}}$ is to ensure zero steady-state error between \mathbf{y} and \mathbf{r} . In fact, if $\widehat{\mathbf{K}} \approx \mathbf{K}$, then $\mathbf{W}(0) \approx \mathbf{I}_N$.
- 2) The matrices \mathbf{K}_p and \mathbf{K}_d influence the stiffness and dumping behavior of the closed-loop system, respectively.

In practice, the control action is implemented as the sum of a feedforward term, given by $[\mathbf{K}_p + \widehat{\mathbf{K}}] \mathbf{r}$, and a feedback term, given by $-\mathbf{K}_p - \mathbf{K}_d \mathbf{H}(d) \mathbf{y}$. One sees that the feedback term takes the form of a proportional-derivative (PD) controller. For the reasons outlined in Section I, the PD controller is fully decentralized, which means that both \mathbf{K}_p and \mathbf{K}_d are diagonal. Accordingly, the i th diagonal entries of \mathbf{K}_p and \mathbf{K}_d correspond to the proportional and derivative gains applied to the i th point of the grid, respectively.

Remark 1: The use of the feedforward term in place of an integral term in the control loop, which would permit a completely decentralized control strategy, is to avoid large overshoots in the closed-loop response [20]. It is worth noting that an alternative control architecture that considers the use of a (centralized) integral feedback in place of a pure feedforward term has been recently considered in [21] and [22]. \square

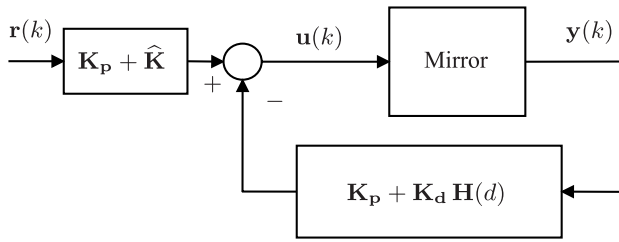


Fig. 6. Equivalent scheme of the internal position control acting on the mirror (shell with actuators and colocated sensors).

Remark 2: The self-tuning mechanism proposed in the following is model free and hence does not rely on (3). The latter, in fact, has been introduced with the only purpose of providing some simple and intuitive motivations for the considered control architecture. Clearly, to capture the complete dynamical behavior of the DM, more elaborated models would be needed (see [34], [35], and the references therein). Nonetheless, similar conclusions concerning the control law (1) could be drawn even when the behavior of the shell is described by the general dynamic equation of a thin plate [34]. \square

B. Control Specifications and Design Issues

The closed-loop system obtained with the digital control action (1) is schematically represented in Fig. 6, where the block denoted as mirror includes the shell, sensors, actuators, and the A/D and D/A interfaces. The control objective is to design $\hat{\mathbf{K}}$, \mathbf{K}_p , and \mathbf{K}_d in such a way that the closed-loop system is stable and satisfies the following specifications when \mathbf{r} is the step input:

- 1) zero steady-state error;
- 2) overshoot less than 10%;
- 3) settling time less than 1 ms, where by settling time, we mean the interval of time needed for \mathbf{y} to remain within $\pm 10\%$ around \mathbf{r} .

As previously noted, zero steady-state error to step inputs can be approximately achieved through a feedforward term by designing $\hat{\mathbf{K}} \approx \mathbf{K}$. This involves estimating the stiffness matrix \mathbf{K} , and is a well-understood problem [24], [25]. On the opposite, the design of the matrices \mathbf{K}_p and \mathbf{K}_d , which are needed to achieve closed-loop stability and satisfy the transient specifications, still poses major challenges. In fact, the design of \mathbf{K}_p and \mathbf{K}_d through a classical model-based paradigm requires, in addition to \mathbf{K} , also the identification of \mathbf{M} and \mathbf{D} , which is, however, a quite challenging task and it is desirable to avoid. As for the LBT, the calibration of the matrices \mathbf{K}_p and \mathbf{K}_d has been executed manually. In addition to relying entirely on the designers' experience, manual calibration is not viable for the next generation of telescopes, which will be equipped with thousands of actuator/sensor pairs.

In [20], an automatic procedure for the calibration of the matrices \mathbf{K}_p and \mathbf{K}_d was proposed. The approach consists of an identification-for-control procedure: first, an estimate of the plant dynamics is determined using *prediction error* methods; then, an *internal model control* design routine determines the

feedback gains in such a way that the transfer matrix from \mathbf{r} to \mathbf{y} is close to a prescribed reference one. To improve the accuracy, an iterative strategy based on the *windsurfer approach* is adopted. The procedure in [20] though effective exhibits a number of deficiencies. First, the identification step might be difficult and time consuming. In addition, it consists of a local parameter tuning: for each radial region (which includes a prespecified number of rings), the calibration procedure involves just one single actuator/sensor pair, which is taken as a representative of the region, and the resulting parameters are then applied to all the remaining pairs belonging to the same region. The choice of such a pair requires specific tests on the shell dynamics. Moreover, due to its local nature, the calibration procedure does not consider the interactions among different points of the shell. As a result, the overall control action need not be fully satisfactory.

In the sequel, a novel approach for tuning the feedback matrices \mathbf{K}_p and \mathbf{K}_d is described. Compared with [20], the considered approach has the following advantages:

- 1) It is *model-free*, i.e., the control design procedure does not require the identification of a model describing the shell dynamics.
- 2) It is *global* in the sense that it views the multiple-input multiple-output system dynamics and its interactions as a whole, which avoids the need for designing each local control unit separately.

III. SELF-TUNING DESIGN OF THE DECENTRALIZED FEEDBACK CONTROLLER

The considered approach follows a *reference model* design paradigm: one first selects a transfer matrix expressing the desired map from \mathbf{r} to \mathbf{y} ; then, matrices \mathbf{K}_p and \mathbf{K}_d are obtained by minimizing, over their entries, a suitable cost function that reflects the discrepancy between actual and desired reference-to-output map. In this respect, let $\mathbf{W}^r(d)$ be the discrete-time transfer matrix expressing the desired closed-loop behavior from \mathbf{r} to \mathbf{y} . Note that the choice of a linear map from \mathbf{r} to \mathbf{y} is due to the fact that control goals such as overshoot and settling time can be translated into transfer functions in a straightforward manner, and further this choice simplifies the analysis of the closed-loop system behavior.

Both the control specifications and the reference model should be representative of an achievable reference-to-output behavior. This invariably requires some information about the shell dynamics. Nonetheless, as detailed in Section V, this information can be obtained from elementary considerations about the structure of the shell, and the identification step is restricted to basic features such as static gain, time constants, and delay. More arguments concerning the choice of $\mathbf{W}^r(d)$ will be provided in Section V-A.

The considerations regarding the cost function to optimize and algorithm details are discussed in Sections III-A and III-B, respectively.

A. Optimization Criterion

We now describe the considered control design procedure for the decentralized feedback action.

Consider parameter-dependent matrices

$$\mathbf{K}_{p,\theta} := \text{diag}\{\theta_1, \dots, \theta_N\} \quad (5)$$

$$\mathbf{K}_{d,\theta} := \text{diag}\{\theta_{N+1}, \dots, \theta_{2N}\} \quad (6)$$

where $\theta_1, \dots, \theta_{2N}$ are all freely assignable scalars, which are grouped into $\theta := \text{col}(\theta_1, \dots, \theta_{2N})$. In accordance with the configuration of Fig. 6, the control design objective is to select θ in such a way that the closed-loop behavior from \mathbf{r} to \mathbf{y} obtained with $\mathbf{K}_{p,\theta}$ and $\mathbf{K}_{d,\theta}$ resembles the behavior specified by $\mathbf{W}^r(d)$ as closely as possible. Some basic considerations [34] suggest to restrict the optimization procedure to

$$\Theta = \{\theta : \theta_i \in \mathbb{R}_{>0}; \quad i = 1, \dots, N\} \quad (7)$$

i.e., to PD controllers with positive proportional gains. This is not strictly necessary for the developments of this paper but sensibly simplifies the analysis.

The considered optimization procedure originates from the so-called *unfalsified control*. Specifically, it relies on the following ideas.

- 1) For any $\theta \in \Theta$, the potential performance of the resulting controller can be evaluated by resorting to a fictitious reference, which associates a *virtual experiment* with the controller [27].
- 2) The controller parameters are selected in such a way that the closed-loop behavior associated with the virtual experiment resembles, as closely as possible, the reference behavior dictated by $\mathbf{W}^r(d)$.

The latter idea was originally introduced in [30] and [31] in the context of adaptive switching control of SISO plants and later extended to the MIMO case in [32]. In this paper, however, the different objective (off-line controller tuning instead of on-line controller adaptation) as well as the peculiarity of the control architecture under study leads to specific analysis and results.

Consider a user-defined $T \in \mathbb{N}$ and let

$$\mathcal{D}_T := \{\mathbf{z}(k); \quad k = 0, \dots, T\} \quad (8)$$

where $\mathbf{z} := \text{col}(\mathbf{u}, \mathbf{y})$, be a set of experimental input-output data collected from the shell (mirror block in Fig. 6). The details on how \mathcal{D}_T can be collected are given in Section V. Define

$$\mathbf{G}_\theta := \mathbf{K}_{p,\theta} + \widehat{\mathbf{K}} \quad (9)$$

$$\mathbf{T}_\theta(d) := \mathbf{K}_{p,\theta} + \mathbf{K}_{d,\theta} \mathbf{H}(d). \quad (10)$$

The matrix $\widehat{\mathbf{K}}$ is positive definite by construction. Thus, also \mathbf{G}_θ is positive definite for all $\theta \in \Theta$. This makes it possible to uniquely compute the parameter-dependent signal \mathbf{r}_θ which solves the following:

$$\mathbf{G}_\theta \mathbf{r}_\theta(k) = \mathbf{u}(k) + \mathbf{T}_\theta(d) \mathbf{y}(k) \quad (11)$$

for $k = 0, \dots, T$.

As depicted in Fig. 7, \mathbf{r}_θ is the hypothetical reference signal that would have produced the data set \mathcal{D}_T , had \mathbf{G}_θ and $\mathbf{T}_\theta(d)$ been in the control loop during the entire time period over which \mathcal{D}_T was collected. The introduction of \mathbf{r}_θ makes it

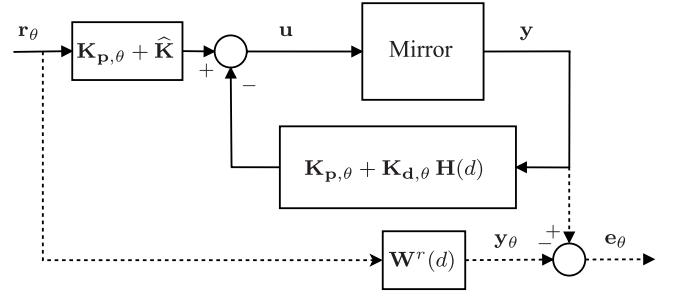


Fig. 7. Virtual experiment associated with a given parameter vector θ and the computation of $\mathcal{E}_{T,\theta}$.

possible to infer the closed-loop behavior corresponding to any given θ . Let

$$\mathbf{e}_\theta(k) := \mathbf{y}(k) - \mathbf{W}^r(d) \mathbf{r}_\theta(k).$$

Then $\mathcal{E}_{T,\theta} := \{\mathbf{e}_\theta(k); k = 0, \dots, T\}$ provides a measure of the closed-loop performance achievable by θ with respect to the desired reference behavior $\mathbf{W}^r(d)$. These considerations suggest to search for the controller parameters vector θ minimizing $\mathcal{E}_{T,\theta}$ in some suitably defined norm.

For reasons that are discussed in Section IV, the considered optimization criterion actually includes also the process input signal \mathbf{u} . Specifically, we associate the parameter-dependent signals with \mathbf{r}_θ

$$\mathbf{y}_\theta(k) := \mathbf{W}^r(d) \mathbf{r}_\theta(k) \quad (12)$$

$$\mathbf{u}_\theta(k) := \mathbf{G}_\theta \mathbf{r}_\theta(k) - \mathbf{T}_\theta(d) \mathbf{y}_\theta(k) \quad (13)$$

for $k = 0, \dots, T$. The control design problem is then casted as the problem of finding the vector

$$\theta_* := \arg \min_{\theta \in \Theta} \|(\mathbf{z} - \mathbf{z}_\theta)|_{[0,T]}\|^2 \quad (14)$$

where $\mathbf{z}_\theta := \text{col}(\mathbf{u}_\theta, \mathbf{y}_\theta)$ and where, given a vector-valued sequence $\{\mathbf{x}(k)\}_{k \in \mathbb{N}_0}$, we define $\|\mathbf{x}\|_{[0,T]}^2 := \sum_{k=0}^T \|\mathbf{x}(k)\|^2$, in which $\|\cdot\|$ stands for the Euclidean norm.

B. Algorithm Details

Some notation is first introduced. Given a vector $\mathbf{x} \in \mathbb{R}^n$ and a scalar-valued function $f(\cdot, \mathbf{x})$, we denote by $\partial f / \partial \mathbf{x}_i$ the partial derivative of f with respect to the i th entry of \mathbf{x} and define

$$\nabla_{\mathbf{x}} f(\mathbf{x}) := \text{col}(\partial f / \partial \mathbf{x}_1, \dots, \partial f / \partial \mathbf{x}_n)' \quad (15)$$

where $\nabla_{\mathbf{x}} f(\bar{\mathbf{x}}) := \nabla_{\mathbf{x}} f(\mathbf{x})|_{\mathbf{x}=\bar{\mathbf{x}}}$. Given a vector $\mathbf{x} \in \mathbb{R}^n$ and a matrix $\mathbf{M} \in \mathbb{R}^{m \times n}$, we denote by \mathbf{x}_i , $[\mathbf{M}]_{(i,:)}$, and $[\mathbf{M}]_{(:,i)}$ the i th entry of \mathbf{x} , and the i th row and column of \mathbf{M} , respectively. Given a vector $\mathbf{x} \in \mathbb{R}^n$ and a vector-valued function $\mathbf{f}(\mathbf{x})$, we let $\nabla_{\mathbf{x}} \mathbf{f}(\mathbf{x}) := \mathbf{F}(\mathbf{x})$ where $[\mathbf{F}(\mathbf{x})]_{(i,:)} = \nabla_{\mathbf{x}} \mathbf{f}_i(\mathbf{x})$. Given a transfer matrix $\mathbf{M}(d)$, a left matrix fraction description (MFD) of $\mathbf{M}(d)$ is denoted by $\mathbf{M}(d) = \mathbf{V}^{-1}(d) \mathbf{U}(d)$, where $\mathbf{V}(d)$ and $\mathbf{U}(d)$ are polynomial matrices. Similar definitions apply to right MFDs [36].

The data set \mathcal{D}_T is collected via a closed-loop experiment using an arbitrary stabilizing controller. This is needed since the shell has nonasymptotically stable open-loop dynamics.

This is because the shell is controlled by means of voice-coil force actuators, which keep the shell in magnetic levitation. This type of control, thanks to the weak constraint given by the support, allows the shell to also attain rigid deformations (Tip and Tilt modes). These deformation modes are, however, characterized by open-loop transfer functions with a pole in 0 in continuous time [20, Sec. 3].

As discussed in Section V, a simple proportional controller is sufficient for stabilizing the shell dynamics. Let θ° denote the parameter vector related to such a stabilizing controller. The vector θ° , along with \mathcal{D}_T , determines the algorithm initialization. Given \mathcal{D}_T , θ° , and a user-defined stopping criterion, the vector of controller parameters is updated in accordance with an iterative gradient-descent algorithm

$$\theta^{[m+1]} = \theta^{[m]} + \gamma^{[m]} \nabla_\theta \|(\mathbf{z} - \mathbf{z}_{\theta^{[m]}})|_{[0,T]}\|^2 \quad (16)$$

initialized from $\theta^{[0]} := \theta^\circ$, where $\theta^{[m]}$ represents the value of θ at the m th iteration and $\gamma^{[m]}$ is a vector with positive entries that represents the step size at the m th iteration.

Some comments on the computation of (16) are in order.

First note that

$$\begin{aligned} \nabla_\theta \|(\mathbf{z} - \mathbf{z}_\theta)|_{[0,T]}\|^2 \\ = -2 \sum_{k=0}^T [\mathbf{z}(k) - \mathbf{z}_\theta(k)]' \begin{bmatrix} \nabla_\theta \mathbf{u}_\theta(k) \\ \nabla_\theta \mathbf{y}_\theta(k) \end{bmatrix}. \end{aligned} \quad (17)$$

Consider now a left MFD of $\mathbf{W}^r(d)$

$$\mathbf{W}^r(d) = \mathbf{Q}^{-1}(d)\mathbf{N}(d) \quad (18)$$

where $\mathbf{Q}(d)$ and $\mathbf{N}(d)$ have a strictly Schur greatest common left divisor (gcd) [36]. Recall now that the transfer matrix $\mathbf{H}(d)$ appearing in the feedback controller can be written as $\mathbf{H}(d) = H(d)\mathbf{I}_N$, where $H(d)$ is the discrete approximation of (2). We can therefore write $\mathbf{H}(d) = \mathbf{R}^{-1}(d)\mathbf{S}(d)$, where $\mathbf{R}(d) = r(d)\mathbf{I}_N$ and $\mathbf{S}(d) = s(d)\mathbf{I}_N$, and where $r(d)$ and $s(d)$ are polynomials such that $H(d) = s(d)/r(d)$ with $r(d)$ strictly Schur. Note that $\mathbf{R}(d)$ commutes with any matrix of the same dimension since it is diagonal with entries on the diagonal equal to one another. Accordingly, consider the following left MFD of $\mathbf{T}_\theta(d)$:

$$\mathbf{T}_\theta(d) = \mathbf{R}^{-1}(d)\mathbf{S}_\theta(d) \quad (19)$$

$$\mathbf{S}_\theta(d) := \mathbf{K}_{p,\theta} + \mathbf{K}_{d,\theta}\mathbf{S}(d). \quad (20)$$

In accordance with (11)–(13), and omitting the arguments d and k for conciseness, \mathbf{z}_θ is computed solving the following set of difference equations:

$$\mathbf{Q}\mathbf{y}_\theta = \mathbf{N}\mathbf{r}_\theta \quad (21)$$

$$\mathbf{R}\mathbf{u}_\theta = \mathbf{R}\mathbf{G}_\theta\mathbf{r}_\theta - \mathbf{S}_\theta\mathbf{y}_\theta \quad (22)$$

$$\mathbf{R}\mathbf{r}_\theta = \mathbf{R}\mathbf{G}_\theta^{-1}\mathbf{u} + \mathbf{G}_\theta^{-1}\mathbf{S}_\theta\mathbf{y} \quad (23)$$

under zero initial conditions.

As for $\nabla_\theta \mathbf{z}_\theta$, it can be computed from the following set of difference equations:

$$\mathbf{Q}\nabla_\theta \mathbf{y}_\theta = \mathbf{N}\nabla_\theta \mathbf{r}_\theta$$

$$\mathbf{R}\nabla_\theta \mathbf{u}_\theta = \mathbf{R}\nabla_\theta \{\mathbf{G}_\theta \mathbf{r}_\theta\} - \nabla_\theta \{\mathbf{S}_\theta \mathbf{y}_\theta\}$$

$$\mathbf{R}\nabla_\theta \mathbf{r}_\theta = \mathbf{R}\nabla_\theta \{\mathbf{G}_\theta^{-1} \mathbf{u}\} + \nabla_\theta \{\mathbf{G}_\theta^{-1} \mathbf{S}_\theta \mathbf{y}\}$$

under zero initial conditions. Given a vector $\mathbf{x} \in \mathbb{R}^n$ and a matrix $\mathbf{M} \in \mathbb{R}^{m \times n}$, it holds that $\mathbf{M}\mathbf{x} = \sum_{i=1}^n [\mathbf{M}]_{(:,i)} \mathbf{x}_i$. Accordingly

$$\nabla_\theta \{\mathbf{G}_\theta^{-1} \mathbf{u}\} = \sum_{i=1}^N \nabla_\theta \{[\mathbf{G}_\theta^{-1}]_{(:,i)}\} \mathbf{u}_i$$

and

$$\begin{aligned} \nabla_\theta \{\mathbf{G}_\theta^{-1} \mathbf{S}_\theta \mathbf{y}\} &= \mathbf{G}_\theta^{-1} \sum_{i=1}^N \nabla_\theta \{[\mathbf{S}_\theta]_{(:,i)}\} \mathbf{y}_i \\ &+ \sum_{i=1}^N \nabla_\theta \{[\mathbf{G}_\theta^{-1}]_{(:,i)}\} \Phi_i \end{aligned}$$

where $\Phi := \mathbf{S}_\theta \mathbf{y}$.

Remark 3: As for the computational complexity of the proposed approach, note that all the computations are performed offline, since the proposed tuning procedure does not require any additional experiment on the true plant. Moreover, while in general, the optimization problem (14) involves a number of variables equal to $2N$ (i.e., twice the number of actuators), in practice, the number of optimization variables can be substantially reduced by subdividing the mirror in a certain number, say M , of radial regions and considering the same gains for all the points belonging to the same radial region. If we further consider a generic step of the gradient-descent algorithm (16), the most computational expensive operation is clearly the computation of the virtual reference \mathbf{r}_θ in (11), which requires the solution of a linear system of N equations and hence the factorization of the matrix \mathbf{G}_θ (for instance, general-purpose algorithms for computing the LU factorization requires less than N^3 operations). With this respect, for applications involving a large number of actuators, it would be interesting to investigate how to exploit the specific structure of the matrix \mathbf{G}_θ so as to speed up the computations.

IV. DISCUSSION

A number of arguments can be put in favor of the considered design procedure. First, it is *model free*, i.e., it does not require the identification of a model describing the shell dynamics, and the optimization is carried out directly over the controller parameters space. Second, it is *global* in the sense that it views the multiple-input multiple-output system dynamics and its interactions as a whole, which avoids the need for designing each local control unit separately. Third, it is *batch wise*. In fact, while the optimization procedure is iterative, each iteration step relies on the same data set \mathcal{D}_T , thus reducing at minimum the interaction with the process. For a comparison between the approach taken here and other approaches to model-free control design in the context of pure centralized feedback, the interested readers are referred to [37].

As for the specific choice of the optimization criterion, some comments are in order. An intuitive justification for (14) is self-evident: suppose $\mathbf{z}_\theta(k) = \mathbf{z}(k)$ for $k = 0, \dots, T$. We then have

$$\mathbf{y}(k) = \mathbf{W}^r(d) \mathbf{r}_\theta(k)$$

$$\mathbf{u}(k) = \mathbf{G}_\theta \mathbf{r}_\theta(k) - \mathbf{T}_\theta(d) \mathbf{y}_\theta(k)$$

for $k = 0, \dots, T$. Since \mathbf{u} and \mathbf{y} are the input–output data related to the actual process dynamics, this implies that \mathbf{G}_θ and \mathbf{T}_θ achieve the desired reference-to-output mapping with respect to \mathbf{r}_θ over the control horizon T . Though \mathbf{r}_θ need not coincide with the reference \mathbf{r} used during normal operation, it is obtained from a stable filtering of \mathbf{u} and \mathbf{y} . Thus, one expects that \mathbf{r}_θ will be sufficiently informative over the frequency range of interest whenever \mathcal{D}_T is such.

A perhaps more concrete justification for (14) is that it derives from explicit *robust* stability considerations. One difficulty with model-free techniques regards the stability of the resulting closed-loop system. In model-based techniques, stability can be inferred simply by analyzing the identified model. On the opposite, model-free techniques cannot take the advantage of this information so that stability should be properly reflected in the optimization criterion. As shown hereafter, under a linearity assumption, this is indeed the case for the cost function in (14).

We assume that the dynamics of the shell are described by a linear time-invariant discrete-time system. For example, this can result from the sampled-data version of (3) or the general equation of a thin plate [20, Sec. 3] after applying an FEM for considering the boundary conditions on the plate dynamics. With this in mind, let $\mathbf{P}(d)$ denote the transfer matrix of the system. Consider next left and right MFDs of $\mathbf{P}(d)$

$$\mathbf{P}(d) := \mathbf{V}^{-1}(d)\mathbf{U}(d) \quad (24)$$

where \mathbf{V} and \mathbf{U} are polynomial matrices with a strictly Schur gclid. Using the quantities introduced in Section III-B, let

$$\mathbf{V}_\theta(d) := \mathbf{Q}(d)\mathbf{R}(d) - \mathbf{N}(d)\mathbf{G}_\theta^{-1}\mathbf{S}_\theta(d) \quad (25)$$

$$\mathbf{U}_\theta(d) := \mathbf{N}(d)\mathbf{G}_\theta^{-1}\mathbf{R}(d). \quad (26)$$

Note that both $\mathbf{V}_\theta(d)$ and $\mathbf{U}_\theta(d)$ are the polynomial matrices since $\mathbf{N}(d)$, $\mathbf{Q}(d)$, $\mathbf{R}(d)$ and $\mathbf{S}_\theta(d)$ are polynomial matrices, and \mathbf{G}_θ is independent of d . Finally, define

$$\mathbf{M}_\theta(d) := \mathbf{V}_\theta^{-1}(d)\mathbf{U}_\theta(d). \quad (27)$$

Note that $\mathbf{M}_\theta(d)$ satisfies $\mathbf{V}_\theta(d)\mathbf{y}_\theta(k) = \mathbf{U}_\theta(d)\mathbf{u}_\theta(k)$ by construction, where \mathbf{y}_θ and \mathbf{u}_θ are as in (12) and (13), respectively.

For each θ , $\mathbf{M}_\theta(d)$ implicitly defines an estimate of the process transfer matrix $\mathbf{P}(d)$ based on the reference model $\mathbf{W}^r(d)$ and the controller matrices \mathbf{G}_θ and $\mathbf{T}_\theta(d)$. It turns out that $\mathbf{M}_\theta(d)$ provides information on the stability of the closed-loop system formed by $\mathbf{P}(d)$ and the decentralized controller corresponding to $\mathbf{T}_\theta(d)$.

To see this, observe first that the following result holds.

Proposition 1: Let $\mathbf{M}_\theta(d)$ and $\mathbf{T}_\theta(d)$ be as in (27) and (19), respectively. Then, the closed-loop system resulting from the feedback interconnection of $\mathbf{M}_\theta(d)$ and $\mathbf{T}_\theta(d)$ is internally stable.

Proof: For conciseness, we omit the arguments d and k . Consider the following polynomial matrix:

$$\mathbf{\Xi}_\theta := \mathbf{V}_\theta\mathbf{R} + \mathbf{U}_\theta\mathbf{S}_\theta \quad (28)$$

whose determinant equals the characteristic polynomial of the closed-loop system formed by \mathbf{M}_θ and \mathbf{T}_θ . We then have

$$\mathbf{\Xi}_\theta = (\mathbf{Q}\mathbf{R} - \mathbf{N}\mathbf{G}_\theta^{-1}\mathbf{S}_\theta)\mathbf{R} + (\mathbf{N}\mathbf{G}_\theta^{-1}\mathbf{R})\mathbf{S}_\theta = \mathbf{Q}\mathbf{R}^2 \quad (29)$$

since we recall that \mathbf{R} commutes with any matrix with the same dimension. This proves the claim since \mathbf{Q} and \mathbf{R} are stable by construction. \square

We now turn back on the feedback interconnection formed by $\mathbf{P}(d)$ and $\mathbf{T}_\theta(d)$. Let $\tilde{\mathbf{U}}_\theta(d) := \mathbf{U}(d) - \mathbf{U}_\theta(d)$ and $\tilde{\mathbf{V}}_\theta(d) := \mathbf{V}_\theta(d) - \mathbf{V}(d)$. The following result holds true.

Proposition 2: Let $\mathbf{P}(d)$ and $\mathbf{T}_\theta(d)$ be as in (24) and (19), respectively. Consider the closed-loop system formed by the feedback interconnection of $\mathbf{P}(d)$ and $\mathbf{T}_\theta(d)$. Let $\mathbf{z} := \text{col}(\mathbf{u}, \mathbf{y})$ be a set of experimental data collected from $\mathbf{P}(d)$ and let $\mathbf{z}_\theta := \text{col}(\mathbf{u}_\theta, \mathbf{y}_\theta)$, where \mathbf{y}_θ and \mathbf{u}_θ are as in (12) and (13), respectively. Then

$$\mathbf{z} - \mathbf{z}_\theta = \Phi_\theta(d) \Delta_\theta(d) \mathbf{z} \quad (30)$$

where

$$\Phi_\theta(d) := \begin{bmatrix} -\mathbf{S}_\theta(d) \\ \mathbf{R}(d) \end{bmatrix} \mathbf{\Xi}_\theta^{-1}(d), \quad \Delta_\theta(d) := [\tilde{\mathbf{U}}_\theta(d) \quad \tilde{\mathbf{V}}_\theta(d)]$$

where $\mathbf{U}_\theta(d)$ and $\mathbf{V}_\theta(d)$ are as in (27).

Proof: We omit again arguments d and k . Using $\mathbf{Q}\mathbf{y}_\theta = \mathbf{N}\mathbf{r}_\theta$ and the definitions of \mathbf{U}_θ , \mathbf{V}_θ , \mathbf{T}_θ , and \mathbf{r}_θ , we have

$$\begin{aligned} \mathbf{Q}\mathbf{R}\mathbf{y}_\theta &= \mathbf{N}\mathbf{R}\mathbf{r}_\theta \\ &= \mathbf{U}_\theta\mathbf{G}_\theta\mathbf{r}_\theta \\ &= \mathbf{U}_\theta\mathbf{u} + \mathbf{U}_\theta\mathbf{T}_\theta\mathbf{y} \\ &= \mathbf{U}_\theta\mathbf{u} + \mathbf{N}\mathbf{G}_\theta^{-1}\mathbf{S}_\theta\mathbf{y} \\ &= \mathbf{U}_\theta\mathbf{u} + \mathbf{Q}\mathbf{R}\mathbf{y} - \mathbf{V}_\theta\mathbf{y}. \end{aligned} \quad (31)$$

Since by hypothesis $\mathbf{V}\mathbf{y} = \mathbf{U}\mathbf{u}$, the above equality can be rewritten as

$$\mathbf{Q}\mathbf{R}(\mathbf{y} - \mathbf{y}_\theta) = \mathbf{V}_\theta\mathbf{y} - \mathbf{U}_\theta\mathbf{u} \quad (32)$$

$$= (\mathbf{V}_\theta - \mathbf{V})\mathbf{y} - (\mathbf{U}_\theta - \mathbf{U})\mathbf{u} \quad (33)$$

and, using $\mathbf{\Xi} = \mathbf{Q}\mathbf{R}^2$, as

$$\mathbf{y} - \mathbf{y}_\theta = \mathbf{R}\mathbf{\Xi}_\theta^{-1}[\tilde{\mathbf{U}}_\theta \quad \tilde{\mathbf{V}}_\theta]\mathbf{z}. \quad (34)$$

By resorting to right MFDs, one can obtain an analog expression for $\mathbf{u} - \mathbf{u}_\theta$. Let $\bar{\mathbf{P}} := \bar{\mathbf{U}}\bar{\mathbf{V}}^{-1}$ and $\bar{\mathbf{M}}_\theta := \bar{\mathbf{U}}_\theta\bar{\mathbf{V}}_\theta^{-1}$ be the right MFDs of \mathbf{P} and \mathbf{M}_θ , respectively, with the $\bar{\mathbf{V}}$, $\bar{\mathbf{U}}$, $\bar{\mathbf{V}}_\theta$, and $\bar{\mathbf{U}}_\theta$ polynomial matrices having the strictly Schur greatest common right divisor. Consider the following polynomial matrix:

$$\Psi_\theta := \mathbf{R}\bar{\mathbf{V}}_\theta + \mathbf{S}_\theta\bar{\mathbf{U}}_\theta \quad (35)$$

whose determinant equals the characteristic polynomial of the closed-loop system formed by \mathbf{M}_θ and \mathbf{T}_θ . Note that due to the particular structure of \mathbf{R} , the matrices \mathbf{R} and \mathbf{S}_θ simultaneously provide both the left and right MFDs of \mathbf{T}_θ . Now, it holds that

$$\bar{\mathbf{V}}_\theta\Psi_\theta^{-1}\mathbf{S}_\theta = \mathbf{S}_\theta\mathbf{\Xi}_\theta^{-1}\mathbf{V}_\theta \quad (36)$$

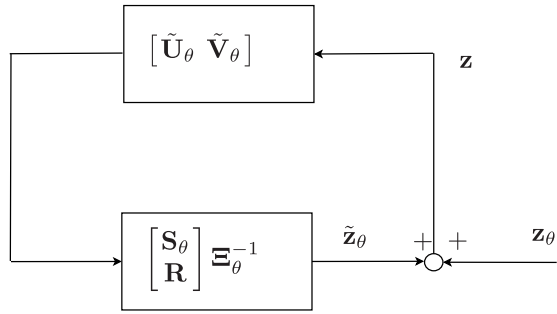


Fig. 8. Pictorial representation of Proposition 2.

since

$$\begin{aligned}
 \mathbf{S}_\theta \mathbf{V}_\theta^{-1} \boldsymbol{\Xi}_\theta &= \mathbf{S}_\theta \mathbf{V}_\theta^{-1} (\mathbf{V}_\theta \mathbf{R} + \mathbf{U}_\theta \mathbf{S}_\theta) \\
 &= \mathbf{S}_\theta \mathbf{R} + \mathbf{S}_\theta \tilde{\mathbf{U}}_\theta \tilde{\mathbf{V}}_\theta^{-1} \mathbf{S}_\theta \\
 &= \mathbf{S}_\theta \mathbf{R} + (\boldsymbol{\Psi}_\theta - \mathbf{R} \tilde{\mathbf{V}}_\theta) \tilde{\mathbf{V}}_\theta^{-1} \mathbf{S}_\theta \\
 &= \boldsymbol{\Psi}_\theta \tilde{\mathbf{V}}_\theta^{-1} \mathbf{S}_\theta.
 \end{aligned} \tag{37}$$

Using (13) and the definitions of \mathbf{U}_θ , \mathbf{V}_θ , \mathbf{T}_θ , and \mathbf{r}_θ , we then have

$$\begin{aligned}
 \mathbf{u}_\theta &= \mathbf{G}_\theta \mathbf{r}_\theta - \mathbf{S}_\theta \mathbf{R}^{-1} \mathbf{y}_\theta \\
 &= \mathbf{G}_\theta \mathbf{r}_\theta - \mathbf{S}_\theta \tilde{\mathbf{U}}_\theta \mathbf{R}^{-1} \tilde{\mathbf{V}}_\theta^{-1} \mathbf{u}_\theta \\
 &= \mathbf{G}_\theta \mathbf{r}_\theta - (\boldsymbol{\Psi}_\theta - \mathbf{R} \tilde{\mathbf{V}}_\theta) \mathbf{R}^{-1} \tilde{\mathbf{U}}_\theta^{-1} \mathbf{u}_\theta \\
 &= \tilde{\mathbf{V}}_\theta \boldsymbol{\Psi}_\theta^{-1} \mathbf{R} \mathbf{G}_\theta \mathbf{r}_\theta \\
 &= \tilde{\mathbf{V}}_\theta \boldsymbol{\Psi}_\theta^{-1} (\mathbf{R} \mathbf{u} + \mathbf{S}_\theta \mathbf{y}) \\
 &= \tilde{\mathbf{V}}_\theta \boldsymbol{\Psi}_\theta^{-1} \mathbf{R} \mathbf{u} + \mathbf{S}_\theta \boldsymbol{\Xi}_\theta^{-1} \mathbf{V}_\theta \mathbf{y} \\
 &= \tilde{\mathbf{V}}_\theta \boldsymbol{\Psi}_\theta^{-1} \mathbf{R} \mathbf{u} + \mathbf{S}_\theta \boldsymbol{\Xi}_\theta^{-1} \mathbf{U} \mathbf{u} + \mathbf{S}_\theta \boldsymbol{\Xi}_\theta^{-1} \tilde{\mathbf{V}}_\theta \mathbf{y}
 \end{aligned} \tag{38}$$

where the last equality follows since $\mathbf{V} \mathbf{y} = \mathbf{U} \mathbf{u}$ by hypothesis. Finally, note that

$$\begin{aligned}
 \mathbf{I}_N - \tilde{\mathbf{V}}_\theta \boldsymbol{\Psi}_\theta^{-1} \mathbf{R} &= \mathbf{I}_N - \tilde{\mathbf{V}}_\theta \boldsymbol{\Psi}_\theta^{-1} \mathbf{R} \tilde{\mathbf{V}}_\theta \tilde{\mathbf{V}}_\theta^{-1} \\
 &= \mathbf{I}_N - \tilde{\mathbf{V}}_\theta \boldsymbol{\Psi}_\theta^{-1} (\boldsymbol{\Psi}_\theta - \mathbf{S}_\theta \tilde{\mathbf{U}}_\theta) \tilde{\mathbf{V}}_\theta^{-1} \\
 &= \tilde{\mathbf{V}}_\theta \boldsymbol{\Psi}_\theta^{-1} \mathbf{S}_\theta \tilde{\mathbf{U}}_\theta \tilde{\mathbf{V}}_\theta^{-1} \\
 &= \tilde{\mathbf{V}}_\theta \boldsymbol{\Psi}_\theta^{-1} \mathbf{S}_\theta \mathbf{V}_\theta^{-1} \mathbf{U}_\theta \\
 &= \mathbf{S}_\theta \boldsymbol{\Xi}_\theta^{-1} \mathbf{U}_\theta.
 \end{aligned} \tag{39}$$

Hence, we immediately get

$$\mathbf{u} - \mathbf{u}_\theta = -\mathbf{S}_\theta \boldsymbol{\Xi}_\theta^{-1} [\tilde{\mathbf{U}}_\theta \ \tilde{\mathbf{V}}_\theta] \mathbf{z} \tag{40}$$

which concludes the proof. A pictorial representation of the relation (30) is given in Fig. 8. \square

It is then straightforward to see that the choice of (14) is strictly related to robust stability considerations. In particular, since $\boldsymbol{\Xi}_\theta(d)$ is strictly Schur, classical small gain arguments indicate that $\|\Phi_\theta(d) \Delta_\theta(d)\|_\infty < 1$ is a sufficient condition for the closed-loop stability of $\mathbf{P}(d)$ in feedback with $\mathbf{T}_\theta(d)$, where $\|\cdot\|_\infty$ denotes the standard \mathcal{H}_∞ norm. Thus, the problem of achieving closed-loop stability can be approached as the problem of minimizing with respect to θ the cost function

$$J(\theta, T) := \frac{\|(\Phi_\theta(d) \Delta_\theta(d) \mathbf{z})|_{[0, T]}\|^2}{\|\mathbf{z}|_{[0, T]}\|^2} \tag{41}$$

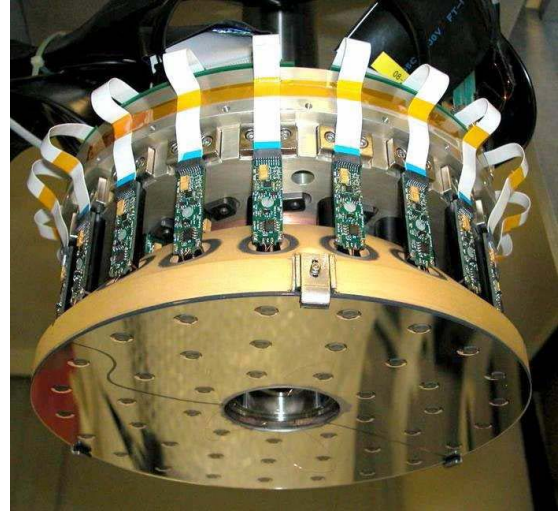


Fig. 9. Prototype with 45 actuators (P45).

which is indeed equivalent to solving (14) for all θ, T , and patterns \mathbf{z} .

In close analogy with Remark 3, we point out that here the assumption of system linearity has the only purpose of providing insights into the features of the considered cost function. Being model free, the considered approach does not require such an assumption.

Remark 4: As a final remark, note that depending on the choice of the reference model $\mathbf{W}^r(d)$, a parameter θ achieving the closed-loop stability condition $\|\Phi_\theta(d) \Delta_\theta(d)\|_\infty < 1$ may exist or not. For instance, if $\mathbf{W}^r(d)$ can be exactly achieved for some choice of θ , then the same θ will also ensure that $\Delta_\theta(d) = 0$. This consideration points out the importance of selecting a reference model $\Delta_\theta(d)$ that is as compatible as possible with the actually achievable closed-loop dynamics.

V. VALIDATION BY AN EXPERIMENTAL SETUP ON PROTOTYPE WITH 45 ACTUATORS

The experimental tests on a prototype with 45 actuators, called P45, reproducing the three innermost rings of one ASM of the LBT [38], are reported. Fig. 9 shows a lateral view of P45, where one can note the actuators distribution on three rings: 21 actuators for the external rings, and 15 and 9 for the central and internal rings, respectively. The considerations regarding the closed-loop dynamics of the shell are discussed in Section V-B. The choice of the reference model and experimental results are given in Sections V-A and V-C, respectively.

A. Choice of the Reference Model

Even if the reference model $\mathbf{W}^r(d)$ can be freely assigned, a convenient form is that of a diagonal or diagonally dominant matrix [39, Sec. 21.6]. In fact, as detailed in the next section, the behavior dictated by $\mathbf{W}^r(d)$ should guarantee a satisfactory level of *modal decoupling* of the shell dynamics. In the sequel, we will restrict ourselves to reference models in a diagonal form.

Note that the possibility of approximately achieving a diagonal dominant behavior is justified in view of the

particular structure of the problem under consideration. This can be intuitively explained by considering once again the approximate finite-dimensional model (3). In fact, a model of the form (3) can be obtained, for example, by means of the FEM. In this case, the matrices \mathbf{M} , \mathbf{D} , \mathbf{K} are sparse and banded, and hence, the closed-loop transfer matrix $\mathbf{W}(s)$ in (4) turns out to be an off-diagonally decaying matrix (see [40] and the references therein).

Let $\mathbf{W}_{(i,j)}^r(d)$ be the transfer function corresponding to the (i, j) th entry of $\mathbf{W}^r(d)$, which characterizes the response at the i th position to the j th control action. The more general choice for $\mathbf{W}^r(d)$ according to a diagonal form is the following:

$$\mathbf{W}^r(d) = \text{diag}\{\mathbf{W}_{(1,1)}^r(d), \dots, \mathbf{W}_{(N,N)}^r(d)\} \quad (42)$$

with $\mathbf{W}_{(i,i)}^r(d)$, $i \in \{1, \dots, N\}$, the representative of the desired closed-loop behavior for the i th grid point.

For experimental purposes, the reference model $\mathbf{W}^r(d)$ was chosen in a diagonal form, and in particular, the set of actuators was partitioned into two radial regions and two different reference models were selected, one for each radial region. The first reference model involves the actuators of the external ring, and was obtained by discretizing with Tustin the continuous-time transfer function

$$W_E^r(s) = \frac{3150}{s + 3150} e^{-8 \times 10^{-5} s} \quad (43)$$

where the time delay is approximated by a third-order Padé approximation. The second reference model involves the actuators of both central and internal rings and was obtained by discretizing with Tustin the continuous-time transfer function

$$W_I^r(s) = \frac{25 \times 10^6}{(s + 5000)^2} e^{-5 \times 10^{-5} s} \quad (44)$$

using again a third-order Padé approximation. Summing up the matrix $\mathbf{W}^r(d)$, to be used in the algorithm of Section III-A, given $N = 45$, takes the form

$$\mathbf{W}_{(i,j)}^r(d) = \begin{cases} 0, & i \neq j \\ W_E^r(d), & i = j = 1, \dots, 21 \\ W_I^r(d), & i = j = 22, \dots, 45 \end{cases} \quad (45)$$

where $W_E^r(d)$ and $W_I^r(d)$ are the discrete-time versions of (43) and (44), respectively.

The reason for considering two different reference models is to prevent the risk of vibrations of the shell. Note that both models describe an overdamping behavior; however, $W_E^r(s)$ is taken of the first order so as to enforce a higher total damping on the external ring. In fact, close to the external edge, viscous damping is lower than in the center, due to the (nonlinear) edge boundary effects. Hence, to maintain the structural integrity of the shell, it is advisable to enforce a higher total damping on the external ring rather than on the innermost rings. Here, with total damping, we mean the sum of the derivative gain and the viscous damping produced by the film of air trapped between the shell and the reference plate. Due to this choice of the reference models, the derivative gains for the external ring are expected to be greater than the ones for the central and internal rings. The time delays of the two reference models have been set equal to the input–output delays of the mirror in the different rings observed from the available data.

B. Modal Basis Analysis

Before illustrating the experimental results, let us briefly analyze the closed-loop dynamics of the shell also in terms of the so-called *modal basis*. To this end, consider a singular value decomposition of the estimated stiffness matrix $\widehat{\mathbf{K}}$ [20, Sec. 6.1]

$$\widehat{\mathbf{K}} = \mathbf{\Lambda} \mathbf{\Xi} \mathbf{\Upsilon}' \quad (46)$$

where $\mathbf{\Xi}$ is a diagonal matrix, and $\mathbf{\Lambda}$ and $\mathbf{\Upsilon}$ are orthogonal matrices, i.e., $\mathbf{\Lambda} \mathbf{\Lambda}' = \mathbf{\Lambda}' \mathbf{\Lambda} = \mathbf{I}_N$ and $\mathbf{\Upsilon} \mathbf{\Upsilon}' = \mathbf{\Upsilon}' \mathbf{\Upsilon} = \mathbf{I}_N$. All the three matrices are real-valued square, and with the same dimensions as $\widehat{\mathbf{K}}$. The columns λ_i of $\mathbf{\Lambda}$ and v_i of $\mathbf{\Upsilon}$, $i = 1, \dots, N$, form an orthogonal basis of the control action space and the shell displacement space, respectively. In other terms, the columns of $\mathbf{\Upsilon}$ describe static deformation modes of the shell. Hence, let $\mathbf{y}_s(t) = \mathbf{\Upsilon}' \mathbf{y}(t)$ and $\mathbf{r}_s(t) = \mathbf{\Upsilon}' \mathbf{r}(t)$ be the vectors of the *modal coefficients* of the actual and desired shell displacements, respectively. Then, by exploiting the orthogonality of $\mathbf{\Upsilon}$, it is straightforward to see that the transfer matrix $\mathbf{W}_s(s)$ mapping \mathbf{r}_s into \mathbf{y}_s can be obtained by the following static transformation:

$$\mathbf{W}_s(s) = \mathbf{\Upsilon}' \mathbf{W}(s) \mathbf{\Upsilon} \quad (47)$$

starting from the transfer matrix $\mathbf{W}(s)$ previously defined in (4). Similarly, the desired discrete-time closed-loop behavior from \mathbf{r}_s to \mathbf{y}_s associated with the reference model $\mathbf{W}^r(d)$ turns out to be

$$\mathbf{W}_s^r(d) = \mathbf{\Upsilon}' \mathbf{W}^r(d) \mathbf{\Upsilon}. \quad (48)$$

In many circumstances, it is important to require a certain *modal decoupling* of the closed-loop dynamics of the shell. With this respect, note that a fundamental decoupling action of the shell closed-loop dynamics is already provided by the feedforward term in that $\widehat{\mathbf{K}} \approx \mathbf{K}$ ensures *steady-state* local/modal decoupling in that $\mathbf{W}_s(0) = \mathbf{W}(0) \approx \mathbf{I}_N$. However, the choice of a $\mathbf{W}^r(d)$ oriented to achieve *transient-state* modal decoupling is a highly desirable feature able to improve the performance of the ASM. In fact, the AO controller in Fig. 4 implements exactly a modal control and generates, as a command signal to pilot the ASM, the vector \mathbf{r}_s that is then converted to \mathbf{r} by a static transformation of the type $\mathbf{r}(t) = \mathbf{\Upsilon} \mathbf{r}_s(t)$ right before to be injected as an input for the ASM control loop [41], [42]. Hence, when dynamic modal decoupling holds, the shell deforms its shape only by a linear combination of the commanded modes.

Consistently with the above-mentioned arguments, the choice (43)–(45) is indeed oriented to achieve a satisfactory level of modal decoupling of the shell dynamics. To evaluate this, first let us introduce the quantities

$$\mathcal{F}(i, j) := \sup_{k \geq 0} \mathcal{Z}^{-1} \left\{ \mathbf{W}_{s(i,j)}^r(d) \frac{1}{1-d} \right\} \quad (49)$$

where $i, j = 1, 2, \dots, N$ and $\mathcal{Z}^{-1}\{\cdot\}$ indicates the inverse Z -transform. Note that $\mathcal{F}(i, j)$ represents the supremum of the time evolution of the i th modal coefficient in response to

a unit step applied to the j th modal command. Second, let us define the following percentage index:

$$C\% := \max_i \frac{\max_{j \neq i} \mathcal{F}(i, j)}{\mathcal{F}(i, i)} \times 100. \quad (50)$$

With the present choice for the reference model, $C\%$ turns out to be equal to 4.7%, which represents a satisfactory modal decoupling level.

Remark 5: The index (50) seems to be the most suitable in the considered setting, since the commands are generated by the AO controller at about 1 kHz and, hence, turn out to be piecewise constant for the ASM control loop that works at a higher frequency (72 kHz in case of LBT).

C. Experimental Results

The data set \mathcal{D}_T has been constructed starting from the data previously collected on the P45 by the *AO Group, Osservatorio Astrofisico di Arcetri*, for analysis purposes. These data were collected from 45 experiments, one for each mode of the P45. Each experiment, lasting 2288 ms, was performed deactivating the feedforward action and using a simple proportional controller with a sampling frequency 72 kHz for the feedback action, which consists of a diagonal matrix with all diagonal entries equal to 6×10^4 N/m. In each experiment, a single mode of the shell was excited by injecting the signal vector $\mathbf{r}(k) = v_i w(k)$, $i = 1, \dots, N$, where w is discrete-time signal with a constant power spectral density in the frequency range [40, 30 000] Hz, thus including the desired closed-loop bandwidth that is around 1 kHz. This setup proved to be effective for ensuring stability along with a high signal-to-noise ratio with respect to each excited mode.

Using these data, \mathcal{D}_T was constructed in two steps. The first step consists in concatenating the experiments corresponding to the rigid modes, the so-called Tip and Tilt modes. This choice is based on the following considerations.

- 1) Each point of the shell turns out to be sufficiently excited by either Tip or Tilt, since they are disposed along a couple of orthogonal axes on the plane supporting the shell and passing through its center. Hence, Tip and Tilt represent a suitable compromise between the dimension of the data set and uniformity of excitation over the shell surface.
- 2) In practical operating conditions, Tip and Tilt modes are the most important ones in that they contribute by more than 80% to the wave-front error variance induced by the atmospheric turbulence, while the degree of correction obtained with the remaining modes decays very rapidly with the increasing spatial frequency [9].
- 3) Tip and Tilt are the modes characterized by the smallest phase and the smallest bandwidth; hence, satisfying the bandwidth and phase margin specifics for the rigid modes ensures that such specifics are satisfied also for the remaining modes.

As a second step, these data were preprocessed with a low-pass filter resulting from the discretization of

$$L(s) = \frac{1}{(1 + s/\omega_h)^6} \quad (51)$$

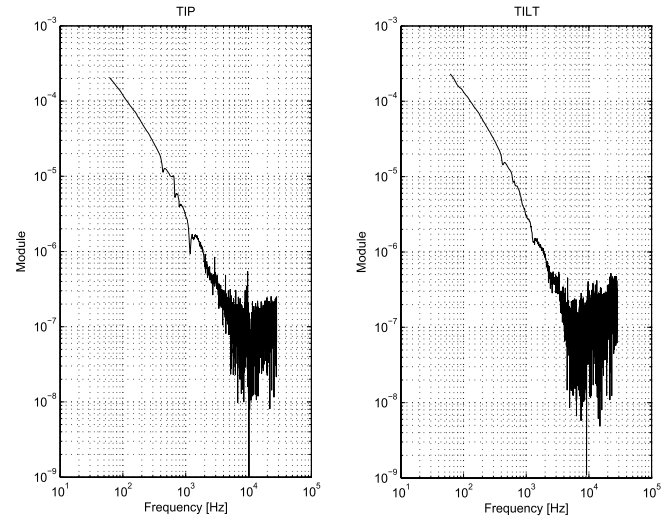


Fig. 10. ETFEs of Tip and Tilt modes.

where $\omega_h = 1$ kHz. The bandwidth of $L(s)$ has been chosen in consideration of the fact that only the experiments concerning Tip and Tilt modes are included in the training set. In fact, for such modes, a cutting frequency of about 1 kHz allows one to attenuate the high-frequency measurement noise while keeping all the information relevant for control design. This can be observed by looking at the plots of the empirical transfer function estimates (ETFEs) of these modes (Fig. 10).

Consistent with the choice of subdividing the actuators set into two radial regions, we have considered the same pair (k_{pE}, k_{dE}) of gains for the external ring and the same pair (k_{pI}, k_{dI}) of gains for the central and internal rings, for a total of four parameters to be tuned. In connection with the notation introduced in Section III-A, this amounts to having $N = 45$ and

$$\theta_i = \begin{cases} k_{pE}, & i = 1, \dots, 21 \\ k_{pI}, & i = 22, \dots, 45 \\ k_{dE}, & i = 46, \dots, 66 \\ k_{dI}, & i = 67, \dots, 90. \end{cases} \quad (52)$$

The gradient-descent algorithm was implemented using the Barzilai–Borwein method [43] with independent step size for P and D gains. The Barzilai–Borwein method proved to compare favorably to a constant step size approach. The algorithm was initialized by letting the P gains equal to $6 \cdot 10^4$ N/m, the D gains equal to 0, and step sizes for P and D gains equal to 10^6 and 100, respectively. A variation of the cost function less than 10^{-10} was chosen as a stopping criterion.

Fig. 11 shows about 1000 iterations of the optimization procedure with the resulting PD gains $k_{pE} = 198340$ N/m, $k_{dE} = 70.86$ Ns/m, $k_{pI} = 106588$ N/m, and $k_{dI} = 36.18$ Ns/m. Accordingly, we let

$$\mathbf{K}_p := \text{diag}\{k_{pE} I_{21}, k_{pI} I_{24}\} \quad (53)$$

$$\mathbf{K}_d := \text{diag}\{k_{dE} I_{21}, k_{dI} I_{24}\}. \quad (54)$$

Figs. 12–17 show the experimental results on the P45 obtained with these matrices. Specifically, the decentralized feedback controller was set equal to $\mathbf{T}(d) = \mathbf{K}_p + \mathbf{K}_d \mathbf{H}(d)$, with $\mathbf{H}(d)$

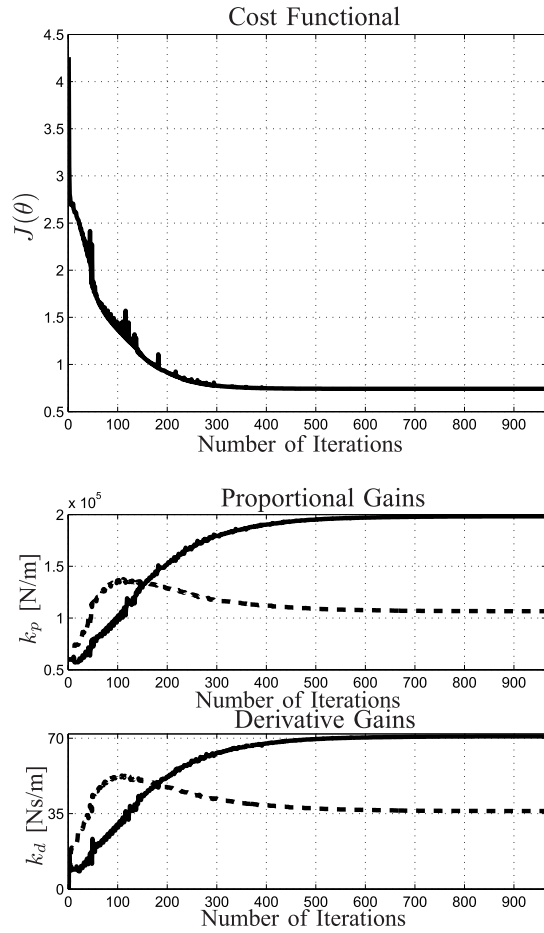


Fig. 11. Tuning algorithm. Top: cost functional. Bottom: PD gains: solid line refers to gains for external ring and dashed line refers to those for central and internal rings. Algorithm stops after 966 iterations, being the rate of variation of cost functional lower than 10^{-10} .

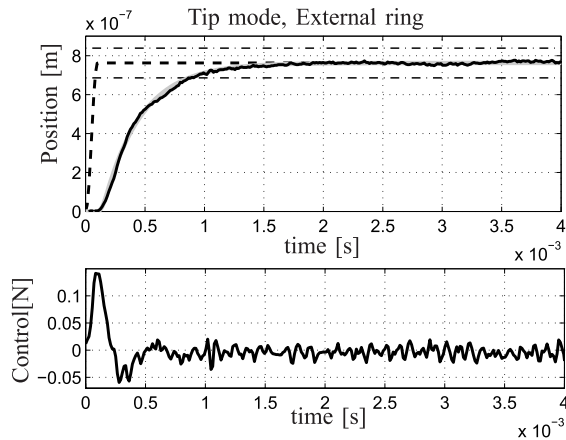


Fig. 12. Local step response related to a single grid point of the external ring. Top: position—reference (dashed line), measured output (solid line), and desired output (gray solid line). Bottom: control action.

as in Section II-A, while the centralized feedforward controller was set equal to $\mathbf{G} = \mathbf{K}_p + \hat{\mathbf{K}}$, where $\hat{\mathbf{K}}$ is the estimate of the P45 stiffness matrix. The control specifications are those described in Section II-B. The experiments were performed by commanding the shell by the signals $\mathbf{r}(k) = v_i g(k)$,

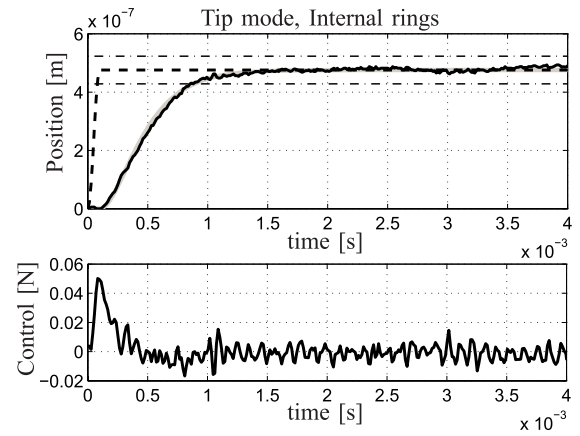


Fig. 13. Local step response related to a single grid point of the internal rings. Top: position—reference (dashed line), measured output (solid line), and desired output (gray solid line). Bottom: control action.

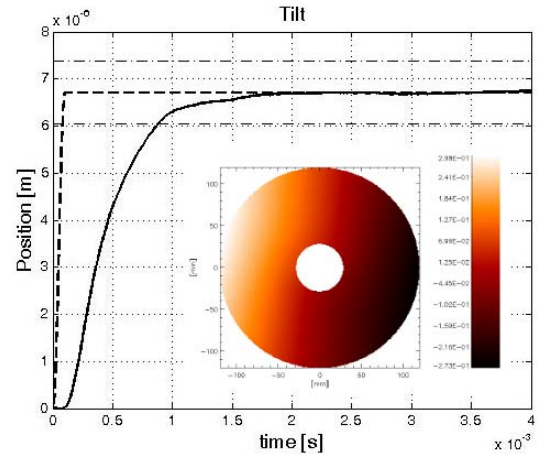


Fig. 14. Modal step response related to Tilt mode: reference (dashed line) and output from the data (solid line).

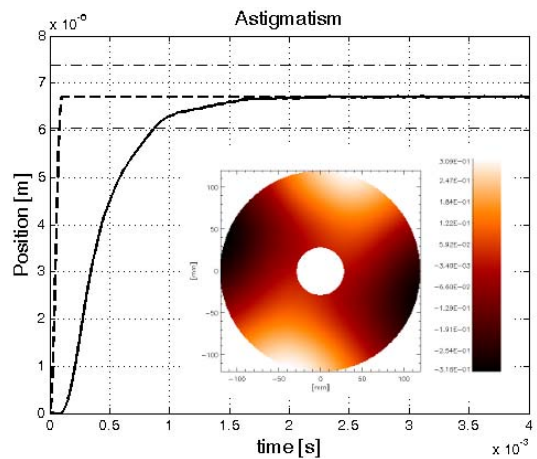


Fig. 15. Modal step response related to Astigmatism mode: reference (dashed line) and output from the data (solid line).

for $i = 1, 2, \dots, 45$ and where g is a discrete-time step. Such a choice corresponds to shaping the shell so as to achieve and keep the configuration of a single static mode for each experiment.

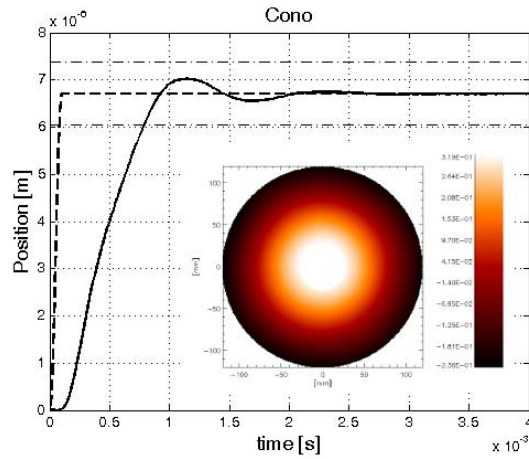


Fig. 16. Modal step response related to Cone mode: reference (dashed line) and output from the data (solid line).

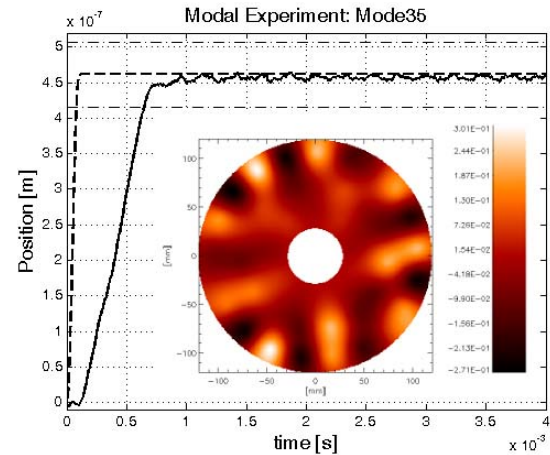


Fig. 18. Modal step response related to Mode 35: reference (dashed line) and output from data (solid line).

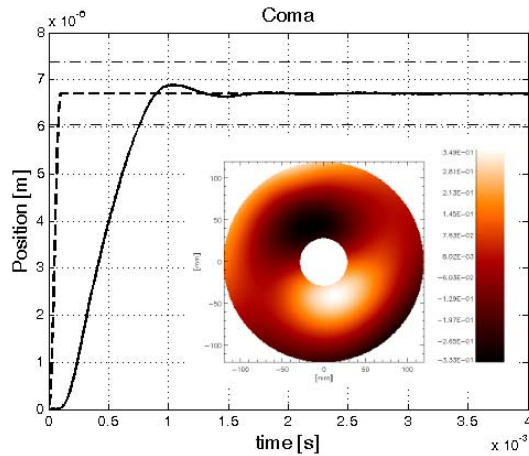


Fig. 17. Modal step response related to Coma mode: reference (dashed line) and output from the data (solid line).

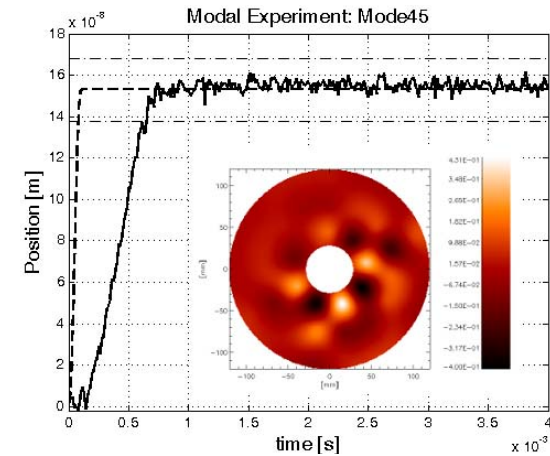


Fig. 19. Modal step response related to Mode 45: reference (dashed line) and output from the data (solid line).

In particular, Figs. 12 and 13 show the displacement of the shell, along with the corresponding control action, of a single grid point related to the experiment wherein the Tip mode is excited. Note that the control specifications are satisfied.

Figs. 14–19 show the time evolution of the modal coefficient $y_{s(m)}(k)$ corresponding to the excited mode m , $m \in \{1, 2, \dots, 45\}$, during the corresponding modal experiment, in other terms $y_{s(m)}(k) = v'_m \mathbf{y}(k)$. In particular, the modes represented in the figures are Tilt, Astigmatism, Cone, Coma, Mode 35, and Mode 45. Modes with high spatial frequency, such as Modes 35 and 45, have no specific name assigned. This is because as pointed out in Section V-C, they contribute much less than modes with low spatial frequency to the correction of atmospheric aberrations in terms of wavefront error variance. In each case, control requirements are completely achieved. In addition, the level of modal decoupling achieved with the matrices (53) and (54) can be measured by the following estimated percentage index:

$$\widehat{C}\% := \max_i \frac{\max_{j \neq i} \widehat{\mathcal{F}}(i, j)}{\widehat{\mathcal{F}}(i, i)} \times 100 \quad (55)$$

where

$$\widehat{\mathcal{F}}(i, j) := \sup_{k \geq 0} \{y_{s(i)}(k)\}_j \quad (56)$$

with $i, j = 1, 2, \dots, N$ and $\{y_{s(i)}\}_j$ denoting the i th component of \mathbf{y}_s associated to the experiment that excites the j th mode. In this case, $\widehat{C}\%$ is equal to 6.6%, which turns out to be very close to the value obtained in Section V-B for the reference model.

As already pointed out, the choice to use only Tip and Tilt modes for the tuning of the PD gains is mainly due to the fact that they are the closest to the instability, while the choice to subdivide the set of actuators in two radial regions has been made in accordance with the typical manual practice. However, the proposed tuning procedure is well suited to being applied also in different settings, e.g., by adding the time histories of some additional modes or by subdividing the set of actuators in a different way. Of course, care must be taken in the choice of the reference model (see also Remark 4), as well as in data pre-filtering so as to attenuate the high-frequency noise due to the electronic devices placed close to the mirror, which is clearly completely uncorrelated with the dynamics of the mirror.

VI. CONCLUSION

ASMs represent a new and extremely promising generation of DMs, consisting of a thin-curved facesheet controlled by means of voice-coil actuators. While ASMs offer several advantages compared with conventional DMs, each actuator needs to be piloted by a dedicated controller, whose parameters must be accurately tuned to obtain the desired mirror shape. At the present time, the tuning of the controllers parameters is executed manually. In this paper, we considered a novel automatic controller tuning procedure that does not rely on the modeling of the ASM dynamics. The effectiveness of the considered approach has been investigated both theoretically and empirically. In the latter regard, the experimental tests on a prototype reproducing the three innermost rings of the LBT ASM have been reported.

REFERENCES

- [1] R. Ragazzoni, "Pupil plane wavefront sensing with an oscillating prism," *J. Modern Opt.*, vol. 43, no. 2, pp. 289–293, 1996.
- [2] L. A. Poyneer and B. Macintosh, "Spatially filtered wave-front sensor for high-order adaptive optics," *J. Opt. Soc. Amer. A*, vol. 21, no. 5, pp. 810–819, 2004.
- [3] S. K. Saha, *Diffraction-Limited Imaging With Large and Moderate Telescopes*. Singapore: World Scientific, 2007.
- [4] C. Correia, H.-F. Raynaud, C. Kulcsár, and J.-M. Conan, "On the optimal reconstruction and control of adaptive optical systems with mirror dynamics," *J. Opt. Soc. Amer. A*, vol. 27, no. 2, pp. 333–349, 2010.
- [5] E. J. Fernández and P. Artal, "Membrane deformable mirror for adaptive optics: Performance limits in visual optics," *Opt. Exp.*, vol. 11, no. 9, pp. 1056–1069, 2003.
- [6] D. Brousseau *et al.*, "Wavefront correction with a ferrofluid deformable mirror: Experimental results and recent developments," *Proc. SPIE, Adapt. Opt. Syst.*, vol. 7015, p. 70153J, Jul. 2008.
- [7] M. Lloyd-Hart, "Thermal performance enhancement of adaptive optics by use of a deformable secondary mirror," *Pub. Astronomical Soc. Pacific*, vol. 112, no. 768, pp. 264–272, 1999.
- [8] A. Riccardi *et al.*, "The adaptive secondary mirror for the Large Binocular Telescope: Results of acceptance laboratory test," *Proc. SPIE, Adapt. Opt. Syst.*, vol. 7015, p. 701512, Jul. 2008.
- [9] A. Riccardi, M. Xompero, and L. Busoni, "Fitting error analysis for the VLT deformable secondary mirror," *Proc. SPIE, Adv. Adapt. Opt. II*, vol. 6272, p. 627240, Jul. 2006.
- [10] G. Brusa and C. Del Vecchio, "Design of an adaptive secondary mirror: A global approach," *Appl. Opt.*, vol. 37, no. 21, pp. 4656–4662, Jul. 1998.
- [11] R. Arsenault *et al.*, "The VLT adaptive optics facility project: Adaptive optics modules," *Messenger*, vol. 123, pp. 11–15, Mar. 2006.
- [12] S. Rabien *et al.*, "The laser guide star program for the LBT," *Proc. SPIE, Adapt. Opt. Syst.*, vol. 7015, p. 701515, Jul. 2008.
- [13] A. Costille, C. Petit, J.-M. Conan, T. Fusco, C. Kulcsár, and H.-F. Raynaud, "Optimization of MCAO performances: Experimental results on ONERA laboratory MCAO bench," *Proc. SPIE, Adapt. Opt. Syst.*, vol. 7015, no. 1, p. 701547, Jul. 2008.
- [14] M. Lloyd-Hart *et al.*, "Adaptive optics for the 6.5-m MMT," *Proc. SPIE, Adapt. Opt. Syst. Technol.*, vol. 4007, p. 167, Jul. 2000.
- [15] F. P. Wildi, G. Brusa, M. Lloyd-Hart, L. M. Close, and A. Riccardi, "First light of the 6.5-m MMT adaptive optics system," *Proc. SPIE, Astronomical Adapt. Opt. Syst. Appl.*, vol. 5169, p. 17, Dec. 2003.
- [16] A. Riccardi *et al.*, "Adaptive secondary mirrors for the Large Binocular Telescope," *Proc. SPIE, Adapt. Opt. Syst. Technol. II*, vol. 4839, p. 721, Feb. 2003.
- [17] D. Gallieni *et al.*, "Voice-coil technology for the E-ELT M4 adaptive unit," presented at the 1st Adapt. Opt. Extremely Large Telescope (AO4ELT) Conf., Jun. 2009, pp. 1–6.
- [18] E. Diolaiti *et al.*, "A preliminary overview of the multiconjugate adaptive optics module for the E-ELT," *Proc. SPIE, Adapt. Opt. Syst.*, vol. 7015, p. 70150U, Jul. 2008.
- [19] N. Hubin *et al.*, "Adaptive optics for extremely large telescopes," *Proc. Int. Astronomical Union*, vol. 1, pp. 60–85, Nov. 2005.
- [20] G. Agapito, S. Baldi, G. Battistelli, D. Mari, E. Mosca, and A. Riccardi, "Automatic tuning of the internal position control of an adaptive secondary mirror," *Eur. J. Control*, vol. 17, no. 3, pp. 273–289, 2011.
- [21] M. Manetti, M. Morandini, and P. Mantegazza, "High precision massive shape control of magnetically levitated adaptive mirrors," *Control Eng. Pract.*, vol. 18, no. 2, pp. 1386–1398, 2010.
- [22] M. Manetti, M. Morandini, and P. Mantegazza, "Self-tuning shape control of massively actuated adaptive mirrors," *IEEE Trans. Control Syst. Technol.*, vol. 22, no. 3, pp. 838–852, May 2014.
- [23] M. Manetti, M. Morandini, P. Mantegazza, R. Biasi, D. Gallieni, and A. Riccardi, "Experimental validation of massively actuated deformable adaptive mirror numerical models," *Control Eng. Pract.*, vol. 20, no. 8, pp. 783–791, 2012.
- [24] G. Brusa-Zappellini *et al.*, "Adaptive secondary mirror for the 6.5-m conversion of the multiple mirror telescope: First laboratory testing results," *Proc. SPIE, Adapt. Opt. Syst. Technol.*, vol. 3762, pp. 38–49, Sep. 1999.
- [25] S. Oberti *et al.*, "Large DM AO systems: Synthetic IM or calibration on sky?" *Proc. SPIE, Adv. Adapt. Opt. II*, vol. 6272, p. 627220, Jun. 2006.
- [26] L. Bakule, "Decentralized control: An overview," *Annu. Rev. Control*, vol. 32, no. 1, pp. 87–98, 2008.
- [27] M. G. Safonov, "Focusing on the knowable," in *Control Using Logic-Based Switching*, A. S. Morse, Ed. Berlin, Germany: Springer-Verlag, 1996, pp. 224–233.
- [28] M. G. Safonov and T.-C. Tsao, "The unfalsified control concept and learning," *IEEE Trans. Autom. Control*, vol. 42, no. 6, pp. 843–847, Jun. 1997.
- [29] R. Wang, A. Paul, M. Stefanovic, and M. G. Safonov, "Cost detectability and stability of adaptive control systems," *Int. J. Robust Nonlinear Control*, vol. 17, nos. 5–6, pp. 549–561, 2007.
- [30] S. Baldi, G. Battistelli, E. Mosca, and P. Tesi, "Multi-model unfalsified adaptive switching supervisory control," *Automatica*, vol. 46, no. 2, pp. 249–259, 2010.
- [31] S. Baldi, G. Battistelli, E. Mosca, and P. Tesi, "Multi-model unfalsified adaptive switching control: Test functionals for stability and performance," *Int. J. Adapt. Control Signal Process.*, vol. 25, no. 7, pp. 593–612, 2011.
- [32] S. Baldi, G. Battistelli, D. Mari, E. Mosca, and P. Tesi, "Multi-model unfalsified adaptive switching control of uncertain multivariable systems," *Int. J. Adapt. Control Signal Process.*, vol. 26, no. 8, pp. 705–722, 2012.
- [33] R. Foy and F.-C. Foy, Eds., "Optics in astrophysics," in *Proceedings of the NATO Advanced Study Institute on Optics in Astrophysics, Cargèse, France from 16 to 28 September 2002* (Series NATO Science Series II: Mathematics, Physics and Chemistry). Dordrecht, The Netherlands: Springer-Verlag, 2005.
- [34] G. Brusa *et al.*, "From adaptive secondary mirrors to extra-thin extra-large adaptive primary mirrors," in *Proc. Backskog Workshop Extremely Large Telescopes*, vol. 57, 2000, pp. 181–201.
- [35] M. Manetti, M. Morandini, and P. Mantegazza, "Servo-fluid-elastic modeling of contactless levitated adaptive secondary mirrors," *Comput. Mech.*, vol. 50, no. 1, pp. 85–98, 2012.
- [36] E. Mosca, *Optimal, Predictive, and Adaptive Control*. Englewood Cliffs, NJ, USA: Prentice-Hall, 1995.
- [37] G. Battistelli, D. Mari, D. Selvi, and P. Tesi, "Unfalsified approach to data-driven control design," in *Proc. 53rd IEEE Conf. Decision Control*, Dec. 2014, pp. 6003–6008.
- [38] A. Riccardi *et al.*, "Adaptive secondary mirrors for the Large Binocular Telescope," *Proc. SPIE, Astronomical Adapt. Opt. Syst. Appl.*, vol. 5169, p. 159, Dec. 2003.
- [39] G. C. Goodwin, S. F. Graebe, and M. E. Salgado, *Control System Design*. Englewood Cliffs, NJ, USA: Prentice-Hall, 2001.
- [40] A. Haber and M. Verhaegen, "Subspace identification of large-scale interconnected systems," *IEEE Trans. Autom. Control*, vol. 59, no. 10, pp. 2754–2759, Oct. 2014.
- [41] G. Agapito, F. Quirós-Pacheco, P. Tesi, A. Riccardi, and S. Esposito, "Observer-based control techniques for the LBT adaptive optics under telescope vibrations," *Eur. J. Control*, vol. 17, no. 3, pp. 316–326, 2011.
- [42] G. Agapito, G. Battistelli, D. Mari, D. Selvi, A. Tesi, and P. Tesi, "Frequency based design of modal controllers for adaptive optics systems," *Opt. Exp.*, vol. 20, no. 24, pp. 27108–27122, 2012.
- [43] J. Barzilai and J. M. Borwein, "Two-point step size gradient methods," *IMA J. Numer. Anal.*, vol. 8, no. 1, pp. 141–148, 1988.



Giorgio Battistelli received the Laurea degree in electronics engineering and the Ph.D. degree in robotics from the University of Genoa, Genoa, Italy, in 2000 and 2004, respectively.

He was a Research Associate with the Dipartimento di Informatica, Sistemistica e Telematica, University of Genoa, from 2004 to 2006. He has been with the University of Florence, Florence, Italy, since 2006, where he is currently an Associate Professor of Automatic Control with the Dipartimento di Ingegneria dell'Informazione.

His current research interests include adaptive and learning systems, real-time control reconfiguration, linear and nonlinear estimation, hybrid systems, sensor networks, and data fusion.

Dr. Battistelli is also an Editor of the *IFAC Journal Engineering Applications of Artificial Intelligence*, an Associate Editor of the *IEEE TRANSACTIONS ON NEURAL NETWORKS AND LEARNING SYSTEMS*, and a member of the Conference Editorial Boards of the *IEEE Control Systems Society* and the *European Control Association*.



Daniele Mari received the B.Sc. degree in mechanical engineering, the M.Sc. degree in automatic control engineering, and the Ph.D. degree in systems science and control engineering from the University of Florence, Florence, Italy, in 2006, 2009, and 2012, respectively.

During his Ph.D. period, he was a Visiting Scholar with the University of Wyoming, Laramie, WY, USA, and he collaborated with the Osservatorio Astrofisico di Arcetri. Thereafter, he held a post-doctoral position with the University of Calabria, Cosenza, Italy, and he has been focused on automotive control. He is currently

with Positech Consulting s.r.l., Milan, Italy, and he works as a Consultant at Ferrari S.p.A, Direzione Power Unit-Elettronica, Modena, Italy, where he is involved in the development of control strategies of the power unit. His current research interests include data-driven control, adaptive switching control, adaptive optics, and automotive control.



Armando Riccardi received the Laurea degree in physics from the Università di Firenze, Florence, Italy, in 1996.

He collaborated to develop and test the prototypes and the final unit of the adaptive secondary mirror for MMT Italia, Tivoli, Italy, and Steward Observatory, University of Arizona, Tucson, AZ, USA, from 1998 to 2001. He was involved in the development, characterization, and commissioning of the large binocular telescope (LBT) adaptive optics system, and in particular, the LBT adaptive secondary mirror,

from 2001 to 2013. He is also participating to the development of adaptive optics systems for some of the main astronomical telescopes, such as LBT, very large telescope, european extremely large telescope, and giant magellan telescope. He has been with the Adaptive Optics Group, Osservatorio Astrofisico di Arcetri, Florence, since 1996, where he is currently a Permanent Senior Researcher.



Pietro Tesi received the Laurea degree and the Ph.D. degree in computer and control engineering from the University of Florence, Florence, Italy, in 2005 and 2010, respectively.

He held a post-doctoral position with the University of Genoa, Genoa, Italy. He was with the automation industry on the research and development of networked SCADA systems. He has been a Visiting Scholar with the University of California at Santa Barbara, Santa Barbara, CA, USA. He has been an Assistant Professor with the Faculty of

Mathematics and Natural Sciences, University of Groningen, Groningen, The Netherlands, since 2014. His current research interests include adaptive control, hybrid systems, networked control, and adaptive optics.

Dr. Tesi is also an Associate Editor of the *IEEE Control Systems Society Conference Editorial Board*.